UC Berkeley
UC Berkeley Previously Published Works

Title

On the strength and fracture toughness of an additive manufactured CrCoNi medium-entropy alloy

Permalink

Authors

Kumar, Punit

Michalek, Matthew

Cook, David H

et al.

Publication Date

DOI

Copyright Information

Peer reviewed

On the strength and fracture toughness of an additive manufactured CrCoNi medium-entropy alloy

Punit Kumar[1,2*], Matthew Michalek[1*], David H. Cook[1,2], Huang Sheng[3], Kwang B. Lau[4], Pei Wang[4], Mingwei Zhang[1,2], Andrew M. Minor[1,2,5] , Upadrasta Ramamurty[3,4], Robert O. Ritchie[1,2#]

[1]Department of Materials Science and Engineering, University of California, Berkeley, CA, USA
[2]Materials Sciences Division, Lawrence Berkeley National Laboratory, Berkeley, CA, USA

[3]School of Mechanical and Aerospace Engineering, Nanyang Technological University, Singapore

[4]Institute of Materials Research and Engineering, Agency for Science, Technology and Research (A∗STAR), Singapore
[5]National Center for Electron Microscopy, Molecular Foundry, Lawrence Berkeley National Laboratory, Berkeley, CA, USA

[*]Authors with equal contribution; [#]Corresponding author

Abstract

An additively manufactured (nominally equiatomic) CrCoNi alloy was processed by laser powder bed fusion (LPBF). At ambient temperatures (298 K), this medium-entropy alloy displayed a yield strength, σ_y of ~691 ± 9 MPa, and an ultimate tensile strength, σ_u of ~926 ± 15.2 MPa; at cryogenic temperatures (77K), yield and tensile strengths increased respectively to σ_y ~ 944 ± 6 MPa and σ_u ~ 1382 ± 11 MPa. These strength levels are 57% and 44% higher than that of the wrought alloy, due to strengthening from the solidification cellular structures intertwined with dislocations in the LPBF CrCoNi. The crack-initiation fracture toughness, K_{JIc} was measured to be ~183.7 ± 28 MPa√m at 298 K; this value marginally decreased by ~4% to ~176 ± 11 MPa√m at 77 K. These K_{JIc} values of the LPBF CrCoNi were 11% and 35% lower than the wrought CrCoNi alloy at 298K and 77K, respectively. The resistance to crack growth of the LPBF CrCoNi from its hierarchical micro- and meso-structures was evaluated using nonlinear-elastic fracture mechanics by measuring R-curve behavior in the form of the J-integral as a function of crack extension. The specific features of the hierarchical microstructures at different length-scales provide a basis for the strengthening and toughening properties of this additively manufactured medium-entropy alloy. This correlation between the deformation and the hierarchical microstructures at different length-scales may provide future guidance for improving the fracture toughness properties of medium-entropy alloys.

Keywords: medium-entropy alloys; additive manufacture; laser powder bed fusion; mechanical properties; strengthening; toughening

1. Introduction

The "Cantor alloy" and its derivatives, consisting of near equimolar concentrations of Fe, Cr, Mn, Ni, and Co, are a class of face-centered cubic (*fcc*) high- and medium-entropy alloys (H/MEAs) that have been extensively studied for their exceptional fracture resistance, especially at extremely low temperatures [1–5]. Although *fcc* H/MEAs show promise as future structural materials for use at ambient and cryogenic temperatures, their relatively low yield strengths, σ_y, limit their potential for many engineering applications. For example, wrought CrCoNi has a fracture toughness, K_{JIc} of ~207 MPa√m at ambient temperature, which increases to K_{JIc} ~273 MPa√m at 77 K and a record-breaking K_{JIc} ~459 MPa√m at 20 K [6]. However, its yield strength, σ_y, is only 350-440 MPa at 298 K and 657 MPa at 77 K [3,7]. These values are comparable to readily available austenitic stainless steels that also have high fracture toughnesses at these temperatures [8].

The exceptional fracture resistance of CrCoNi is associated with prolonged plastic deformation ahead of the crack tip, which is sustained by a sequence of deformation mechanisms — stacking fault formation, nano-twinning, and at cryogenic temperatures stress-induced *fcc* to hexagonal close packed (*hcp*) phase transformation [3,6]. However, because only substitutional solid-solution strengthening is active in CrCoNi, its yield strength, σ_y, is relatively low. Conventional ways of strengthening metallic materials, *e.g.*, by reducing the grain size or employing precipitation hardening, can be effective but they could adversely affect the fracture toughness due to the inherent conflict between strength and toughness [9,10]. This tradeoff occurs primarily because a high fracture toughness requires sustained plasticity ahead of the crack tip, which can be more easily attained with lower yield strength, σ_y. Conventional strengthening mechanisms that restrict the dislocation mobility can limit the dislocation-assisted blunting of the crack tip, thereby promoting crack extension at relatively lower stress-intensity factors (K). To simultaneously improve the strength and fracture toughness, the movement of dislocations does need to be restricted for strength but not be completely stopped so that they can distribute damage away from the crack tip and preserve fracture resistance.

Additive manufacturing (AM) processes, such as the laser powder bed fusion (LPBF), can provide an alternative microstructural design path to overcoming the strength-toughness tradeoff by introducing micro- and meso-scale structures, which are hierarchical in nature and have been

2

shown to strengthen materials while preserving (and in some instances enhancing) their fracture toughness and damage tolerance [11–13]. These hierarchical structures in the LPBF-processed alloys are a result of the line-by-line and layer-by-layer 'bottom up' manufacturing of the structural components, which are laser scan tracks, melt pools, and solidification cellular structures [11]. The width of the laser scan track and the depth of the melt pool controls the size, morphology, and texture of the grains [13,14]. Solidification cellular structures form due to solute segregation by constitutional undercooling during rapid solidification that is inherent to LPBF [15,16]. Further, because of severe thermal cycling that occurs during the build process, dislocation debris, pinned by the segregated alloying elements, decorate the cell boundaries [17] While the size of these cells can be manipulated in the range of 0.2 to 10 µm by altering the process parameter combinations, their shape can be controlled through the manipulation of the direction of the maximum thermal gradient inside the melt pool [15,18]. These dislocations cells are of interest because they act to strengthen the material by Taylor hardening [19–21]. Additionally, they promote multiple deformation mechanisms and allow the movement of dislocations during the later stage of strain hardening, preserving the material ductility [11,22–25]. In the present study, the tensile and fracture properties of LPBF CrCoNi with a sub-micrometer dislocation cellular structure were examined to investigate the following - (i) the effectiveness of the cellular structures in simultaneous enhancement of strength and fracture toughness of CrCoNi; (ii) whether they can promote crack growth resistance, *i.e.*, R-curve behavior; and (iii) although the CrCoNi alloy fractures by microvoid coalescence that is a strain-controlled process, whether the hierarchical micro- and meso-structures that result from the LPBF process can generate additional extrinsic toughening by imparting tortuosity to the crack path, as has been reported for precipitation hardened and high-strength materials produced by LPBF [26–29].

2. Materials and Methods

CrCoNi blocks of size $25 \times 25 \times 25$ mm^3 were fabricated by the LPBF process using a pre-alloyed powder of Cr, Co, and Ni. The composition of the printed part is listed in Table S1 of the Supplementary Information (SI). The composition (at.%) of Cr (35%), Co (32.6%), and Ni (31.9%) was measured by inductively coupled plasma atomic emission spectroscopy (ICP-AES), S (<0.005%) and C (0.05%) by combustion infrared detections, and O (0.22%) and N (0.025%)

3

by inert gas fusion. The average size (D50) of the powder particles was ~34.6 µm. For the LPBF process, a Trumpf Truprint-1000 machine equipped with a Nd: YAG fiber laser and protective Ar gas environment was used. The optimized set of process parameters for printing the blocks was a laser power of ~150 W, layer thickness of ~20 µm, hatch spacing of ~30 µm, a laser spot size of ~30 µm, and scanning speed of 670 mm/s. The schematic in Fig. 1A illustrates the chessboard scan strategy with an island size of 4×4 mm^2 and interlayer rotation of 67° used to print the specimens. From the as-printed blocks, compact-tension C(T) and dog-bone tensile specimens were machined by wire electrical discharge machining (EDM) with testing orientations perpendicular to build direction, as shown in Fig. 1B. The dimensions of the C(T) and tensile specimens are shown in Figs. 1C and D, respectively. Uniaxial tensile and fracture toughness measurements were performed at room temperature (298 K) and in a liquid nitrogen bath (77 K). Before testing, the tensile specimens were ground with SiC paper on all sides to remove the oxide layer that forms during the EDM process. Three tensile specimens each were tested at room temperature (298 K) and 77 K. Uniaxial tensile tests were performed at a strain rate of 10^{-3} s^{-1} with a servo-hydraulic 810 MTS load frame (MTS Corp., Eden Prairie, MN, USA) operated using an Instron 8800 digital controller (Instron Corp., Norwood, MA, USA) following the ASTM Standard E8 [30]. The strain was measured using a clip-on extensometer attached to the specimens. The yield strength, σ_y, ultimate tensile strength (UTS), σ_u, and elongation to fracture, e_f, were determined from the uniaxial tensile engineering stress-strain curves. The true stress-strain (σ–ε) curves were estimated from engineering stress-strain (S-e) data using the equations: $\varepsilon = \ln(1 + e)$ and $\sigma = S(1 + e)$. Strain hardening exponents, n, for each temperature, were determined according to the constitutive law, $\sigma = \kappa\varepsilon^n$, where κ is a scaling constant.

Compact-tension specimens, with $W = 18$ mm in width and $B = 10$ mm in thickness, were machined from as the printed blocks. In total, three C(T) specimens were tested at each ambient (298 K) and cryogenic (77 K) temperature. These specimens were electrical discharge machined (EDM) with a V-notch of root radius, ρ ~150 µm. These notches were further sharpened with a razor blade to a ~20 to 60 µm root radius to minimize the load required for crack initiation during the fatigue pre-cracking process. Additionally, the specimens were mechanically polished to a mirror finish for monitoring the crack growth during fatigue cracking using a long-distance microscope equipped with a camera. The fatigue pre-cracking was carried out on a 100 kN

4

servo-hydraulic 810 MTS load frame (MTS Corp., Eden Prairie, MN, USA) operated using an Instron 8800 digital controller (Instron Corp., Norwood, MA, USA). It was performed using a constant amplitude sinusoidal wave of load ratio of $R = 0.1$ at a frequency of 15 Hz. The final pre-crack length was in the range of $a/W = 0.45 - 0.55$, where a is the crack length, and W is the width of the specimen. To ensure that the crack did not significantly deviate from a straight path during fracture toughness testing, specimens were side-grooved up to a depth of ~1.5 mm on each side after the pre-cracking. The fracture toughness tests were performed in displacement control at a crosshead velocity of 0.02 mm/s. The crack length during the fracture tests was monitored by the compliance method from the load-line displacement measured using a clip-on gauge of 3 mm gauge length (Epsilon Technology, Jackson, WY, USA) mounted on the knife edge of the C(T) specimens. The nonlinear-elastic fracture mechanics method recommended in the ASTM Standard E1820 was used for the crack growth and fracture toughness measurements [31]. All the fracture toughness measurements satisfied J-dominance and plane-strain conditions for validity, $i.e.$, $b, B >> 10\ J/\sigma_f$, where b is the uncracked ligament length (W-a), B is the specimen thickness, and $\sigma_f = \frac{\sigma_y + \sigma_u}{2}$. The measured energy release rates, J, were used to estimate the equivalent Mode I fracture toughness from the relationship: $K_{JIc} = (J_{Ic}*E')^{1/2}$, $K_{Jss} = (J_{SS}*E')^{1/2}$, and $E' = \frac{E}{(1-\nu^2)}$, where E is the elastic modulus and ν is the Poisson ratio measured for wrought CrCoNi [3]. The crack-initiation toughness, J_{Ic}, was estimated by the 0.2 mm construction line method described in ASTM E1820; the steady-state (crack-growth) toughness, J_{ss}, was estimated as the J value at the maximum crack extension of ~2 mm allowed for the length of the uncracked ligament, b [31].

Optical and electron microscopes were used to investigate the microstructure of the specimens before and after the fracture tests. For optical microscopy, specimens were polished to a mirror finish and etched by Kalling's reagent to see the melt pool and laser scan tracks. To analyze the microstructure in the fully plane-strain region after the fracture toughness tests, the C(T) specimens were sectioned at mid-thickness, such that each slice had a thickness of B/2. One-half of the specimens tested at 298 and 77 K each were placed in epoxy resin, ground, and polished to a 0.04 μm surface finish using colloidal silica. From the polished half, the microstructure and the crack growth path were characterized using electron back-scattered diffraction (EBSD), performed with a step size of 1 μm. The EBSD data were analyzed using a

commercially available software Aztec Crystal. From the other half of the C(T) specimens, a mid-thickness 0.5 mm thin slice was cut and further thinned down to 50 µm by mechanical polishing to 1200 grit for transmission electron microscopy (TEM). The lowest monotonic plastic zone size, r_p ($\sim 1/2\pi(K_{JIc}/\sigma_y)^2$) was $\sim$5.5 mm for the sample tested at 77 K. Therefore, to sample the deformation mechanism inside the plastic zone, 3 mm diameter discs were punched out near the crack tip from the fractured specimens. The center of these disks was further thinned to make them electron transparent by twin-jet polishing at $-20\,°C$ under a stable current of $\sim$25 mA using a Fischione Model 110 electropolisher, and the electrolyte consisting of 70% methanol, 20% glycerol, and 10% perchloric acid. The deformation mechanism near the crack tip was characterized by the diffraction contrast imaging (DCI) technique on an FEI F20 UT Tecnai STEM under an accelerating voltage of 200 kV. The fracture surfaces of the tensile and C(T) specimens were investigated using a secondary electron detector in a Scios 2 dual beam scanning electron microscope (SEM).

3. Results

3.1. Microstructure

The microstructure of the LPBF CrCoNi is hierarchical in nature with micro- and meso-structural features at three distinct length-scales. First, the melt pool boundary and laser scan tracks are illustrated by the white dotted lines in a representative 3D microstructure displayed in Fig. 2A. Here, the plane parallel to the build direction (BD) shows the laser scan track; the planes perpendicular to the build direction, SD, and TD, show the melt pool boundaries, which are clearly visible in Fig. 2C. The melt-pool depth is 50-100 µm and the width of the laser scan tracks, *h,* is $\sim 69 \pm 9$ µm (Figs. 2A and C). The spacings between melt pool boundaries (Fig. 2C) are not well defined because of the bidirectional scan strategy utilized for melting the layers (Fig. 1A). The dimensions of these meso-structural features are related to the processing parameters, *i.e.*, volumetric energy density $\sim$373 J/mm^3 and laser spot size $\sim$30 µm. Second, Figs. 2B and C show grains growing inside the laser scan tracks and across the melt pool boundaries, respectively. The average size of the grains, *d,* in the plane parallel to the build direction (BD), is $\sim 13 \pm 15$ µm. The inverse pole figure (IPF) map in Fig. 2B shows that the size of the grains is restricted by the width of the laser scan track on the BD plane, producing a synthetic microstructure. However, since the scan strategy varies in each checkerboard island (4×4 mm^2),

6

even though a 67° scan rotation was used between each layer to reduce the microstructural anisotropy [32], the laser scan tracks are differently oriented on each island (Fig. S1 in the Supplementary Materials). Moreover, the laser scan tracks are not well defined everywhere due to the shallow layer thickness of ~20 µm. The microstructure of the LPBF CrCoNi is similar to other *fcc* alloys produced by this additive manufacturing process [20,33]. Figure 2B shows a predominant <110> texture along the build direction with aberrant grains of <100> texture. The volumetric energy density employed in the present study is relatively higher than that used in other studies (60-250 J/mm^3) for the LPBF process of the CrCoNi and Cantor alloys [11,19,34]. Therefore, in the present case, the maximum heat flux direction inside the melt pool is at 45° to the build direction (Fig. 2C), which promotes a <110> texture in the BD plane [28]. However, in the regions where melt pools overlap, aberrant grains of <100> texture (along the build direction) also form (Figs. 2B and C) [33,35]. Additionally, the grains are columnar with <100> texture in the SD and TD planes (Fig. 2B). The columnar grains have an average major and minor axis of ~76 ± 54 µm and ~12 ± 9 µm, respectively (Fig. 2B). Finally, Fig. 2D shows the third microstructural feature in the LPBF CrCoNi, namely the solidification cellular structures with a high density of dislocations intertwined on their boundaries. The size, λ of the cellular structure is ~0.5 ± 0.1 µm. The size of the solidification cells, λ is the primary dendritic arm spacing during solidification. Therefore, the cooling rate during the LPBF process can be estimated by the solidification equation, $\lambda = AC_R^{-\omega}$, where C_R is the cooling rate, and A and ω are constants, and vice versa [36,37]. Using values for A and ω of, respectively, ~148 and 0.38, measured on stainless steel, an approximate cooling rate estimate for the present microstructure is C_R ~ 2.95×10^6 °C/s.

3.2. Mechanical properties

3.2.1. Tensile behavior

The engineering stress, *S, vs.* engineering strain, *e,* responses of the tensile specimens at 298 and 77 K are plotted in Fig. 3A. The yield strength, σ_y of the LPBF CrCoNi was found to be 691 ± 9 MPa at 298 K, which increases to 944 ± 6 MPa at 77 K. Similarly, the ultimate tensile strength, σ_u was measured as 926 ± 15 MPa at 298 K and 1382 ± 11 MPa at 77 K. The elongation to fracture e_f at these temperatures was ~ 38% and 30%, respectively. The representative true stress, σ *vs.* true strain, ε values are plotted in Fig. 3B. The corresponding work hardening, dσ/dε, plots

in Fig. 3B illustrate a relatively higher instantaneous work hardening rate during deformation at 77 K. However, the strain-hardening exponent, n, at both these temperatures is similar, i.e., ~0.19 and ~0.22, respectively. In comparison to wrought CrCoNi, σ_y of the LPBF CrCoNi is ~57% and 44% higher at 298 and 77 K, respectively [3]. Since the strain-hardening exponent of n ~0.19 is significantly lower than ~0.4 for the wrought counterpart, the ultimate tensile strength, σ_u is only ~5% higher than that of the wrought CrCoNi [3]. A relatively low n indicates a loss in the material's ductility since a higher n can serve to delay the onset of instability. The increase in instantaneous strain hardening rate and the yield strength at 77 K is driven by the rise in the Peierls resistance at cryogenic temperature. Moreover, the tensile specimens tested at 298 K show necking before fracture. However, the specimens tested at 77 K fractured before necking. The ultimate tensile strength of LPBF CrCoNi (~1382 ± 11 MPa) at 77 K is similar to another study on LPBF CrCoNi (1306 ± 84 MPa [11]). These results of tensile tests indicate that specimens at 77 K fractured just before necking because of the specimen geometry since the necking phenomenon is highly dependent on the tensile specimen geometries.

SEM fractographs, displayed in Figs. 4A and B, clearly show that the tensile specimens fractured by microvoid coalescence at both temperatures. The sizes of the microvoids were ~0.37 ± 0.17 µm at 298 K and ~0.52 ± 0.25 µm at 77 K. These microvoids are smaller than the value of 2.6 ± 0.7 µm observed in the tensile tested wrought CrCoNi, because it primarily failed after significant necking unlike the LPBF CrCoNi [3]. In the specimen fractured at 77 K, certain regions show voids with a marked elongated morphology that is relatively shallow because of lack of necking before fracture (Fig. S2).

3.2.2. Fracture toughness

The R-curves, in terms of the nonlinear elastic energy release rate, J (kJm^{-2}), as a function of crack extension, Δa (mm), of specimens tested at 298 and 77 K are plotted in Fig. 3C. The average energy release rate at crack initiation, J_{Ic}, was measured to be 135.7 ± 42.7 kJm^{-2} at room temperature (298 K) and 118 ± 14.2 kJm^{-2} at the cryogenic temperature (77 K). The corresponding crack-initiation K_{JIc} values estimated at these temperatures are 183.7 ± 28 MPa√m and 176.3 ± 11 MPa√m, respectively. The material shows rising R-curve behavior at both these temperatures. However, the steady-state (crack-growth) fracture toughness, K_{Jss} at 77 K, is ~238 ± 7 MPa√m, which is ~17 % lower than 287 ± 33 MPa√m measured at 298 K; this indicates that

the R-curve at ambient temperature is steeper than that measured at cryogenic temperature. Overall, the K_{JIc} of the LPBF CrCoNi is 11% and 35% lower than that of the wrought counterpart at 298 and 77 K, respectively (although the R-curve of one specimen tested at 298 K displays a K_{JIc} of ~216 MPa√m and a K_{Jss} of ~ 320 MPa√m, which are comparable to those of the wrought CrCoNi).

Figures 5A and B show the fractographic images of specimens failed by overload. These fracture surfaces have a bimodal distribution of microvoids, with a larger size of ~72 ± 18 µm and smaller size of ~0.4 ±0.2 µm. The larger microvoids are of similar size to the width of laser scan tracks, *i.e., h* ~69 ± 9 µm measured on the BD plane (Fig. 2B). At the bottom of these large microvoids (*e.g.*, at locations II and III in Figs. 5A and B), a cleavage-like fracture is observed, with closely spaced lines, of width ~0.8 ± 0.3 µm, at the surfaces.

4. Discussion

4.1. Strengthening mechanism

The additively manufactured *fcc* alloys have relatively high yield strength, σ_y, compared to the conventionally manufactured counterparts because of their solidification cellular structure with entangled dislocations [13]. The dislocations in the cellular boundaries dissociate and form stacking faults, which provide a strong barrier to the movement of dislocations [16]. However, the ductility of these alloys remains nominally unaffected because the cell boundaries allow movement of partials and promote nano-twinning during the plastic deformation [11,19,23]. These cells, however, are less effective barriers to dislocation movement than high-angle grain boundaries, especially if their size is small (< 0.5 µm) [11,38]. Therefore, the strengthening from these cellular structures is considered to follow Taylor hardening by dislocation forest, *i.e.*, yield strength, viz: [11,20,39,40].

$$\sigma_y = \sigma_{fr} + K_y \times d^{-0.5} + \alpha MGb\sqrt{\rho}, \tag{1}$$

where σ_{fr} ~ 218 MPa is the frictional stress from the lattice and the solute to the movement of dislocations [41,42], K_y ~ 537 MPa√µm is the Hall-Petch constant signifying the strength of the grain boundary as the barrier to dislocation movement [42], d ~13 ± 15 µm is the average grain size in the BD plane, *i.e.*, perpendicular to the tensile loading direction, α is an empirical correction factor ~ 0.4 for *fcc* materials, M is the Taylor factor ~2.27-3.67 (Fig. S1), G is the

9

shear modulus ~ 87 GPa [11], *b* is the Burgers vector of a perfect dislocation (*a*/2<110>) ~2.52 Å [11], and ρ is the dislocation density. The dislocation density can be roughly estimated from the width of dislocation cell boundaries, *t* ~ 90 nm (Fig. 2D), where $\sqrt{\rho} = 1/t$ [40,43]. Using these parameters and constants, the estimated σ_y is in the range of ~587-725 MPa for a Taylor factor *M* ~2.27-3.67 (Fig. S1). The measured σ_y ~ 691 ± 9 MPa, lies within this predicted range, confirming that one of the primary strengthening mechanisms is Taylor hardening from the dislocation cells. Based on the estimated value of σ_y, the contribution of dislocation cellular structures to the strengthening is on the order of ~38 to 50% at 298 K. At 77 K, σ_y of the LPBF CrCoNi increases by ~37%; in contrast, the difference in the yield strength of wrought CrCoNi, is ~49% at these temperatures. Although the strength of the LPBF CrCoNi at 77 K is ~44% higher compared to wrought CrCoNi, the marginal drop in the increase of σ_y at 77 K indicates a relatively lower contribution of the dislocation cellular structure to strengthening at 77 K. Assuming that the yield strength increases at 77 K because of the higher Peierls resistance to dislocation movement, which should be similar for both conventionally manufactured and LPBF CrCoNi, the strength of dislocation cells as a barrier to the movement of dislocations likely to have weakened at lower temperatures.

4.2. Toughening mechanisms

The K_{JIc} values of the LPBF CrCoNi are 11% and 35% lower than the wrought CrCoNi alloy at 298 and 77 K, respectively. Nevertheless, the impressive combination of a yield strength of ~1 GPa and a fracture toughness of ~176 MPa$\sqrt{m}$ make the LPBF CrCoNi a contender for structural application at cryogenic temperatures; furthermore, it solves the problem of the low yield strength of the wrought CrCoNi alloy. As discussed above, nearly ~44% of the improvement in the yield strength of the LPBF CrCoNi is primarily driven by the dislocation cellular structure, although its K_{JIc} fracture toughness remains largely unaffected. We believe that the preservation of the fracture toughness can be associated with the contribution of its hierarchical structure, as discussed in the following sections.

4.2.1. Intrinsic toughening

The fracture toughness of ductile *fcc* alloys is primarily intrinsic, *i.e.*, the inelastic deformation ahead of the crack distributes the damage away from the crack tip, thereby increasing the energy required to grow the crack [5,13]. While both elastic and plastic deformation contribute to this, in

10

ductile materials such as CrCoNi, the plasticity ahead of the crack tip plays the primary role. To understand the mechanism of plasticity ahead of a crack tip, TEM analysis was carried out on specimens extracted from inside the crack-tip plastic zone. These samples were prepared from the center of the specimens fractured at 298 and 77 K, *i.e.*, from the region under fully plane-strain conditions. TEM images in Figs. 6A and B display the deformation mechanisms ahead of the crack tip at 298 and 77 K, respectively. Figure. 6A shows <111> planar slip cutting through the dislocation cell boundaries at 298 K. The cell boundaries offer resistance to the movement of dislocations, which promotes slip planarity, *i.e.*, dislocations are forced to glide on a limited number of planes [44]. After the pile-up of these dislocations near a cell boundary, the leading dislocation or partials can break through if the stress from the dislocation pile-up crosses a threshold value [45]. After that, because of the relatively low resistance to dislocation movement on these planes, they act as a highway to the movement of dislocations and form slip bands (Fig. 6A) [46]. The planar slip bands in LPBF CrCoNi serve to blunt the crack tip by distributing damage away from the crack tip. However, other deformation mechanisms, *i.e.*, nano-twinning and the extensive formation of stacking faults, which are usually observed during deformation of conventionally and additively manufactured CrCoNi, were not active in the present microstructure, even at 77 K (Fig. 6B) [3,11]. The corresponding diffraction patterns from these locations also indicate the absence of nano-twinning (Fig. S3).

The lack of nano-twinning and extensive stacking fault formation during the plastic deformation of the LPBF CrCoNi is unexpected, particularly in the presence of dislocation cellular structures where the movement of dislocations is restricted. In both the CrCoNi and Cantor alloy produced by LPBF, nano-twins have been observed during their deformation in ambient conditions [11,19]. Further, the critical twinning stress for additively manufactured CrCoNi is 800-900 MPa, which is much lower than the stress encountered by the tensile specimens in the present study [47]. This points to the role of the chemical composition of the material in affecting the deformation mechanisms. For example, the activation of a deformation mechanism is directly linked to the stacking fault energy of the *fcc* alloys, which in turn depends on the alloy composition. Accordingly, a detailed compositional analysis of the current printed parts was performed, of which the notable findings were: (i) the LPBF CrCoNi parts had ~2 at.% higher Cr than the equiatomic composition, and (ii) their composition contained 0.22 at.% interstitial O. A higher Cr composition reduces the stacking fault energy of CrCoNi, which

should promote additional deformation mechanisms [48]. For example, stress-induced transformation in conjunction with twinning is observed during the deformation of $Cr_{40}CoNi$ [49] Therefore, the most likely reason for the absence of the additional deformation mechanisms is the presence of interstitial O (0.22 at.%), which could have been picked up during the LPBF process. Interstitials such as O and N are known to increase the stacking fault energy of *fcc* materials, which can inhibit twinning and affect the dislocation dynamics during deformation [50,51]. To the best of our knowledge, there is a lack of literature showing the effect of interstitial O on the properties of the CrCoNi. Although the effect of C and N interstitials on the strength of conventionally manufactured CrCoNi and CrCoFeMnNi has been investigated, these interstitials also have similar effect on the stacking fault energy and the deformation mechanisms [52]. For example, a ~0.2 at.% C and N, the yield strength increases by <30 MPa [53–55]. However, a significant drop in the fracture toughness is noticed when N composition is ~1.75 at.% [56]. These results indicate that a direct effect of 0.22 at.% O on the tensile strength of LPBF CrCoNi is minimal. However, since the deformation mechanisms twinning and the formation of stacking faults were suppressed, as observed from post-deformation microstructures, the ductility of LPBF CrCoNi is possibly affected. For example, in LPBF CrCoNi, where nano twinning was observed during deformation, the elongation to failure at 77 K was ~45% [57]. Moreover, the fracture toughness of LPBF CrCoNi could have been possibly even higher if intrinsic toughening mechanisms supporting strain hardening, the nano-twinning, and the formation of stacking faults were active [4].

In the absence of the additional deformation mechanisms which are known to enhance the fracture toughness of the wrought CrCoNi, especially at cryogenic temperatures, it is still somewhat remarkable that LPBF CrCoNi maintains its K_{JIc} at 298 and 77 K. For example, compared to room temperature, at 77 K the fracture toughness dropped by merely 4%, while the strength increased by 44%, although, no additional deformation mechanisms were activated at 77 K, as evidenced by post deformation TEM images (Fig. 6B) and the tensile stress-strain plots (Fig. 3B). The work hardening exponents, $n \sim 0.19$ and 0.22 respectively at 298 and 77 K, are also similar. This suggests the presence of additional extrinsic toughening mechanisms induced by the AM-created meso-structures, in addition to the intrinsic toughening driven by dislocation-mediated plasticity.

4.2.2. Extrinsic toughening

To examine the crack path and the influence of the microstructure during fracture, the compact-tension specimens used for fracture toughness tests were sectioned mid-thickness to expose the region of the fracture path predominantly under plane-strain conditions. IPF maps in Figs. 7A and B show the region of crack initiation and subsequent propagation during fracture tests at 298 and 77 K, respectively. These images indicate that the cracks predominantly propagate along the boundaries of the laser scan tracks (indicated by white dotted lines in Fig. 7) as they coincide with the boundaries of the grains inside the scan tracks; this results in a deflected crack path. Since a chessboard scan strategy with an island size of 4×4 mm^2 and interlayer rotation of 67° was used to print the specimens (Fig. 1A), the orientation of the laser scan tracks in front of the crack with respect to the mode-I direction of crack propagation varies across the length, width, and through the thickness of the samples. Therefore, it is difficult to comment on the optimum orientation of laser scan tracks for the highest tortuosity to the crack path. Looking at the microstructure on the surface, the highest fracture toughness, K_{JIc} ~216 MPa√m, was recorded in the specimen where the laser scan tracks were perpendicular to mode-I crack growth direction (Fig. 7A). Further, in another specimen, the crack arrested after growing ~2 mm when it encountered an island with laser scan tracks perpendicular to the mode-I crack growth direction, as indicted by the white dotted lines in Fig. 7C.

For the specimens tested at 77 K, the laser scan tracks are not perpendicular to the direction of crack growth, although even then the crack path is tortuous because the crack prefers to grow along the boundaries of the laser scan tracks (Fig. 7B). This tortuous crack path is indicative of crack deflection by the laser scan tracks which provides a source of (secondary) extrinsic toughening.

The fracture surfaces of the C(T) specimens were also examined to discern whether the tortuous crack paths induced by the laser scan tracks were present throughout the thickness of the specimens. Figures 8A and B show fractographs of the specimens fractured at 298 K and 77 K, respectively. The fracture surfaces of both these specimens have well-defined features of dimensions (94 ± 19 µm) somewhat similar to the width of the laser scan tracks (69 ± 9 µm). Further, their effect seems more prominent during fracture at 77 K, where the number of secondary cracks was relatively higher (Figs. 5B and 8B). These secondary cracks form because

the crack grows preferably along the laser scan track boundaries which are not aligned with the mode-I direction of the crack propagation. The secondary cracks are also present in the stretch zone of the specimen fractured at 77 K, indicating a more effective contribution of extrinsic toughening at 77 K. related to the crack deviation by laser tracks. This may explain why there is only marginal drop (~4%) in toughness of the LPBF CrCoNi at 77 K, although the yield strength increased by 44%. While it is complex to quantitively establish the individual contributions of extrinsic and intrinsic mechanisms in the toughening of LPBF CrCoNi, it can be qualitatively stated that in the absence of a prolonged sequence of deformation mechanisms, including stacking fault formation and nano-twinning, which is the basis of the prolonged strain hardening and exceptional (intrinsic) toughness of the wrought CrCoNi alloy [3], extrinsic toughening by crack deflection and tortuosity, induced by the meso-structures created by LPBF, contributes to the fracture resistance of the LPBF CrCoNi, especially at 77 K.

As noted above, the fractographs of C(T) specimens in Fig. 5 show a bimodal distribution of microvoids of sizes (width) ~72 ± 18 and 0.4 ±0.2 µm. The bottoms of the larger microvoids show a cleavage-like fracture with a pattern of lines spaced at ~0.8 ± 0.3 µm (Figs. 5A and B). The size of the larger microvoids and their location corresponds to the aberrant grains of the <100> texture present along the build direction (Fig. 2B). These anomalous grains form when the solidification cells grow parallel to the build direction, *i.e.*, perpendicular to the loading direction in the C(T) specimens (Fig. 2C). Because these aberrant grains have cellular structures perpendicular to the loading direction, when a void nucleates at the cell boundaries, these grains crack showing traces of the cellular structure in the form of lines on the fracture surface. The average spacing between these lines is ~0.8 ± 0.3 µm, *i.e.*, similar to the average size of the dislocation cells ~0.5 ± 0.1 µm (Fig. 5A-II and B-III). Moreover, most solidification cells grow at a 45° angle to the build direction resulting in a dominant <110> texture along the build direction (Fig 2B). These cells are at a 45° angle to the loading direction; as such, these regions fracture by forming microvoids of size ~0.4 ±0.2 µm (Fig. 5) [33].

4.2.3. Micromechanics model

To determine the characteristic length-scale for the void nucleation and coalescence controlling the fracture toughness of the LPBF CrCoNi, a simple micromechanics model, the stress-state modified critical strain-controlled model for ductile fracture, is used [58]. According to this

model, the fracture toughness, K_{JIc} of a ductile material is related to a critical fracture strain over a characteristic (microstructurally significant) length-scale ahead of the crack tip leading to the onset of crack initiation or instability. LPBF CrCoNi follows a power-law work-hardening model, *i.e.*, $\left(\frac{\bar{\sigma}}{\sigma_o}\right) = \left(\frac{\bar{\epsilon}_p}{\varepsilon_o}\right)^n$, where $\bar{\sigma}$ is the equivalent stress, and $\bar{\epsilon}_p$ is the equivalent plastic strain, σ_o and ε_o are the reference flow stress and strain, respectively, and n is the work hardening exponent. In such materials, assuming that the elasto-plastic HRR strain fields dominate ahead of the crack tip [59,60], the crack initiates when $\bar{\epsilon}_p$ exceeds a critical value $\bar{\epsilon}_f$ over a microstructurally characteristic distance, l_o^*, ahead of the crack tip, as illustrated by the schematics in Fig. 9. In this case, according to the stress-state modified critical strain-controlled model, J_{Ic} can be estimated from Eq. 2 [5,58]:

$$J_{Ic} = \frac{K_{JIc}^2}{E'} \approx \left[\frac{I_n}{\tilde{\varepsilon}_{ij\,(\theta,n)}}\right] \sigma_f \tilde{\epsilon}_f l_o^*. \tag{2}$$

Here E' is $E/(1-\nu^2)$, where E is Young's modulus and ν is Poisson's ratio, $\tilde{\epsilon}_f$ is ductility of the material under triaxial stress conditions (which is usually an order of magnitude smaller than the elongation to failure, e_f, measured by uniaxial tensile tests), and $\left[\frac{I_n}{\tilde{\varepsilon}_{ij\,(\theta,n)}}\right]$ is a dimensionless function of θ and n from the HRR solution [59,60] - for ductile materials such as CrCoNi, in plane strain condition ($\theta \sim 0°- 45°$) $\left[\frac{I_n}{\tilde{\varepsilon}_{ij\,(\theta,n)}}\right]$ is ~100 [5]. Substituting these constants into Eq. 2, the characteristic microstructural length, l_o^* can be estimated as:

$$l_o^* = \frac{J_{Ic}}{\sigma_f \tilde{\epsilon}_f}. \tag{3}$$

From Eq. 3, the estimated values of l_o^* are ~46 ±12 and 33 ±12 µm, respectively, for corresponding fracture toughness measurements at 298 and 77 K. These estimations are of similar order to the width of the laser scan track, h ~69 ± 9 µm and the larger microvoids (~72 ± 18 µm) observed on the fracture surface. Therefore, the estimate from the micromechanics model serves to suggest that the fracture toughness of LPBF CrCoNi is related to the width of laser scan tracks (Fig. 9B) since the resistance to crack growth along their boundaries is relatively lower (Fig. 7).

15

4.2.4. Potential for solving conflict between strength and toughness through AM

Clearly, the dislocation cellular structure strengthens the LPBF CrCoNi alloy; concomitantly, the material is toughened intrinsically through plastic deformation ahead of the crack tip and extrinsically via crack path tortuosity due to the laser scan track/aberrant grains of <110> texture. It is a long-held view that natural materials are processed "bottom-up" into a hierarchical structure which usually gives them a sound combination of strength and toughness since these properties are invariably generated at different length-scales [9]. With conventional manufacturing using "top-down" processing, it is difficult to control the structure at multiple length-scales to introduce such hierarchical features, *e.g.*, to enhance the strength of a material without affecting its toughness. This study demonstrates that hierarchical microstructural features introduced through additive manufacturing of the medium-entropy CrCoNi alloy using laser powder bed fusion processing can readily provide strengthening and without compromising the fracture toughness.

5. Summary and Conclusions

CrCoNi specimens produced by the LPBF process show increased strength compared to conventionally manufactured CrCoNi at 298 K and 77 K. Further, a desirable fracture toughness at 298 K and 77K was preserved despite the significant increase in yield strength. This study illustrates that additive manufacturing (AM) processes could be a viable way of resolving the strength and toughness tradeoff in ductile materials. The following are the key conclusions:

(i) The AM-induced hierarchical microstructure simultaneously strengthens and toughens the LPBF CrCoNi. The yield strength is improved by dislocation cellular structure, whereas the cracks prefer to grow along the laser track boundaries providing extrinsic toughening from the crack path tortuosity.

(ii) The interstitial O picked up during the LPBF processing of CrCoNi appears to inhibit nano-twinning and stacking fault formation during plastic deformation.

(iii) Reducing the number of aberrant grains with <110> texture along the build direction and reducing interstitial O to activate deformation mechanisms nano-twinning and stacking fault formation could further improve the fracture toughness of the LPBF CrCoNi alloy.

Author contributions

P.K. and R.O.R conceived the idea and led the project. H.S., K.W.L., P.W., and U.R. helped with the 3D printing of the specimens. M.M., P.K., and D.H.C. conducted the mechanical testing and microstructural characterization by SEM/EBSD, M.Z. and A.M. provide the microstructural characterization by TEM, and M.M. helped with the preparation of the TEM specimens. P.K and M.M. wrote the manuscript, and R.O.R. helped with editing.

References

[1]   N. Stepanov, M. Tikhonovsky, N. Yurchenko, D. Zyabkin, M. Klimova, S. Zherebtsov, A. Efimov, G. Salishchev, Effect of cryo-deformation on structure and properties of CoCrFeNiMn high-entropy alloy, Intermetallics (Barking). 59 (2015) 8–17. https://doi.org/10.1016/j.intermet.2014.12.004.

[2]   K.V.S. Thurston, B. Gludovatz, A. Hohenwarter, G. Laplanche, E.P. George, R.O. Ritchie, Effect of temperature on the fatigue-crack growth behavior of the high-entropy alloy CrMnFeCoNi, Intermetallics (Barking). 88 (2017) 65–72. https://doi.org/10.1016/j.intermet.2017.05.009.

[3] B. Gludovatz, A. Hohenwarter, K.V.S. Thurston, H. Bei, Z. Wu, E.P. George, R.O. Ritchie, Exceptional damage-tolerance of a medium-entropy alloy CrCoNi at cryogenic temperatures, Nat Commun. 7 (2016) 10602. https://doi.org/10.1038/ncomms10602.

[4] D. Liu, Q. Yu, S. Kabra, M. Jiang, P. Forna-Kreutzer, R. Zhang, M. Payne, F. Walsh, B. Gludovatz, M. Asta, A.M. Minor, E.P. George, R.O. Ritchie, Exceptional fracture toughness of CrCoNi-based medium- and high-entropy alloys at 20 kelvin, Science (1979). 378 (2022) 978–983. https://doi.org/10.1126/science.abp8070.

[5] B. Gludovatz, A. Hohenwarter, D. Catoor, E.H. Chang, E.P. George, R.O. Ritchie, A fracture-resistant high-entropy alloy for cryogenic applications, Science (1979). 345 (2014) 1153–1158. https://doi.org/10.1126/SCIENCE.1254581.

[6] D. Liu, Q. Yu, S. Kabra, M. Jiang, P. Forna-Kreutzer, R. Zhang, M. Payne, F. Walsh, B. Gludovatz, M. Asta, A.M. Minor, E.P. George, R.O. Ritchie, Exceptional fracture toughness of CrCoNi-based medium- and high-entropy alloys at 20 kelvin, Science (1979). 378 (2022) 978–983. https://doi.org/10.1126/science.abp80.

[7] B. Gludovatz, R.O. Ritchie, Fracture properties of high-entropy alloys, MRS Bull. 47 (2022) 176–185. https://doi.org/10.1557/s43577-022-00267-9.

[8] W.J. Mills, Fracture toughness of type 304 and 316 stainless steels and their welds, International Materials Reviews. 42 (1997) 45–82. https://doi.org/10.1179/imr.1997.42.2.45.

[9] R.O. Ritchie, The conflicts between strength and toughness, Nat Mater. 10 (2011) 817–822. https://doi.org/10.1038/nmat3115.

[10] W.-L. Li, J.C.M. Li, The effect of grain size on fracture toughness, Philosophical Magazine A. 59 (1989) 1245–1261. https://doi.org/10.1080/01418618908221173.

[11] B. Han, C. Zhang, K. Feng, Z. Li, X. Zhang, Y. Shen, X. Wang, H. Kokawa, R. Li, Z. Wang, P.K. Chu, Additively manufactured high strength and ductility CrCoNi medium entropy alloy with hierarchical microstructure, Materials Science and Engineering: A. 820 (2021) 141545. https://doi.org/10.1016/j.msea.2021.141545.

[12] S. Wei, C. Hutchinson, U. Ramamurty, Mesostructure engineering in additive manufacturing of alloys, Scr Mater. 230 (2023) 115429. https://doi.org/10.1016/J.SCRIPTAMAT.2023.115429.

[13] T.H. Becker, P. Kumar, U. Ramamurty, Fracture and fatigue in additively manufactured metals, Acta Mater. 219 (2021) 117240. https://doi.org/10.1016/j.actamat.2021.117240.

[14] R. Jayaraj Radhakrishnan, P. Kumar, H.L. Seet, S.M.L. Nai, P. Wang, U. Ramamurty, Cascading of the as-built microstructure through heat treatment and its role on the tensile properties of laser powder bed fused Inconel 718, Materialia. 21 (2022) 101272. https://doi.org/10.1016/j.mtla.2021.101272.

[15] L. Yang, O. Harrysson, D. Cormier, H. West, H. Gong, B. Stucker, Additive manufacturing of metal cellular structures: design and fabrication, JOM. 67 (2015) 608–615. https://doi.org/10.1007/s11837-015-1322-y.

[16] T. Voisin, J.B. Forien, A. Perron, S. Aubry, N. Bertin, A. Samanta, A. Baker, Y.M. Wang, New insights on cellular structures strengthening mechanisms and thermal stability of an austenitic stainless steel fabricated by laser powder-bed-fusion, Acta Mater. 203 (2021) 116476. https://doi.org/10.1016/J.ACTAMAT.2020.11.018.

[17] D. Kong, C. Dong, S. Wei, X. Ni, L. Zhang, R. Li, L. Wang, C. Man, X. Li, About metastable cellular structure in additively manufactured austenitic stainless steels, Addit Manuf. 38 (2021). https://doi.org/10.1016/J.ADDMA.2020.101804.

[18] S.-H. Li, P. Kumar, S. Chandra, U. Ramamurty, Directed energy deposition of metals: processing, microstructures, and mechanical properties, International Materials Reviews. 68 (2023) 605–647. https://doi.org/10.1080/09506608.2022.2097411.

[19] Z.G. Zhu, Q.B. Nguyen, F.L. Ng, X.H. An, X.Z. Liao, P.K. Liaw, S.M.L. Nai, J. Wei, Hierarchical microstructure and strengthening mechanisms of a CoCrFeNiMn high entropy alloy additively manufactured by selective laser melting, Scr Mater. 154 (2018) 20–24. https://doi.org/10.1016/j.scriptamat.2018.05.015.

[20] F. Wei, B. Cheng, P. Kumar, P. Wang, J.J. Lee, H.L. Seng, K.H. Cheong, K.B. Lau, C.C. Tan, A comparative study of additive manufactured and wrought SS316L: Pre-existing dislocations and grain boundary characteristics, Materials Science and Engineering A. 833 (2022). https://doi.org/10.1016/j.msea.2021.142546.

[21] S.H. Li, Y. Zhao, P. Kumar, U. Ramamurty, Effect of initial dislocation density on the plastic deformation response of 316L stainless steel manufactured by directed energy deposition, Materials Science and Engineering A. 851 (2022). https://doi.org/10.1016/j.msea.2022.143591.

[22] P. Kumar, Z. Zhu, S.M.L. Nai, R.L. Narayan, U. Ramamurty, Fracture toughness of 304L austenitic stainless steel produced by laser powder bed fusion, Scr Mater. 202 (2021) 114002. https://doi.org/10.1016/j.scriptamat.2021.114002.

[23] L. Liu, Q. Ding, Y. Zhong, J. Zou, J. Wu, Y.L. Chiu, J. Li, Z. Zhang, Q. Yu, Z. Shen, Dislocation network in additive manufactured steel breaks strength–ductility trade-off, Materials Today. 21 (2018) 354–361. https://doi.org/10.1016/j.mattod.2017.11.004.

[24] P. Agrawal, S. Thapliyal, S.S. Nene, R.S. Mishra, B.A. McWilliams, K.C. Cho, Excellent strength-ductility synergy in metastable high entropy alloy by laser powder bed additive manufacturing, Addit Manuf. 32 (2020) 1–7. https://doi.org/10.1016/j.addma.2020.101098.

[25] Z. Sun, X. Tan, S.B. Tor, C.K. Chua, Simultaneously enhanced strength and ductility for 3D-printed stainless steel 316L by selective laser melting, NPG Asia Mater. 10 (2018) 127–136. https://doi.org/10.1038/s41427-018-0018-5.

[26] J. Suryawanshi, K.G. Prashanth, S. Scudino, J. Eckert, O. Prakash, U. Ramamurty, Simultaneous enhancements of strength and toughness in an Al-12Si alloy synthesized using selective laser melting, Acta Mater. 115 (2016) 285–294. https://doi.org/10.1016/j.actamat.2016.06.009.

[27] M.J. Paul, Q. Liu, J.P. Best, X. Li, J.J. Kruzic, U. Ramamurty, B. Gludovatz, Fracture resistance of AlSi10Mg fabricate d by laser powder b e d fusion, Acta Mater. 211 (2021) 116869. https://doi.org/10.1016/j.actamat.2021.116869.

[28] P. Kumar, O. Prakash, U. Ramamurty, Micro-and meso-structures and their influence on mechanical properties of selectively laser melted Ti-6Al-4V, Acta Mater. 154 (2018) 246–260. https://doi.org/10.1016/j.actamat.2018.05.044.

[29] J.-Y. Xu, P.-C. Zhang, R. Guo, L.-X. Liu, Y.-P. Kang, Z. Liu, C. Zhang, L. Liu, Toughening the additively manufactured Al alloys via manipulating microstructural heterogeneity, (2023). https://doi.org/10.1016/j.jallcom.2023.169322.

[30] ASTM E8, ASTM E8/E8M Standard test methods for tension testing of metallic materials 1, Annual Book of ASTM Standards 4. (2010) 1–27. https://doi.org/10.1520/E0008.

[31] ASTM Standard E1820, Standard test method for measurement of fracture toughness, ASTM Book of Standards. (2013) 1–54. https://doi.org/10.1520/E1820-13.Copyright.

[32] J. Xu, Y. Ding, Y. Gao, H. Wang, Y. Hu, D. Zhang, Grain refinement and crack inhibition of hard-to-weld Inconel 738 alloy by altering the scanning strategy during selective laser melting, Mater Des. 209 (2021) 109940. https://doi.org/10.1016/j.matdes.2021.109940.

[33] K.A. Sofinowski, S. Raman, X. Wang, B. Gaskey, M. Seita, Layer-wise engineering of grain orientation (LEGO) in laser powder bed fusion of stainless steel 316L, Addit Manuf. 38 (2021) 101809. https://doi.org/10.1016/J.ADDMA.2020.101809.

[34] X. Gao, Y. Lu, Laser 3D printing of CoCrFeMnNi high-entropy alloy, Mater Lett. 236 (2019) 77–80. https://doi.org/10.1016/j.matlet.2018.10.084.

[35] F. Yan, W. Xiong, E.J. Faierson, Grain structure control of additively manufactured metallic materials, Materials. 10 (2017) 1260. https://doi.org/10.3390/ma10111260.

[36] M. El-bealy, B. Thomas, Prediction of dendrite arm spacing for low alloy steel casting processes, Mater. Trans. B. 74 (1992) 265–79.

[37] P. Agrawal, S. Thapliyal, P. Agrawal, A. Dhal, R.S. Haridas, S. Gupta, R.S. Mishra, Additive manufacturing of a metastable high entropy alloy: Metastability engineered microstructural control via process variable driven elemental segregation, Materials Science and Engineering A. 872 (2023). https://doi.org/10.1016/J.MSEA.2023.144938.

[38] Z. Li, B. He, Q. Guo, Strengthening and hardening mechanisms of additively manufactured stainless steels: The role of cell sizes, Scr Mater. 177 (2020) 17–21. https://doi.org/10.1016/J.SCRIPTAMAT.2019.10.005.

[39] B.G. I Taylor, R. Society Yarrow Professor, The mechanism of plastic deformation of crystals. Part I.—Theoretical, Proceedings of the Royal Society of London. Series A, Containing Papers of a Mathematical and Physical Character. 145 (1934) 362–387. https://doi.org/10.1098/RSPA.1934.0106.

[40] F.F. Lavrentev, The type of dislocation interaction as the factor determining work hardening, Materials Science and Engineering. 46 (1980) 191.

[41] S. Yoshida, T. Bhattacharjee, Y. Bai, N. Tsuji, Friction stress and Hall-Petch relationship in CoCrNi equi-atomic medium entropy alloy processed by severe plastic deformation and subsequent annealing, Scr Mater. 134 (2017) 33–36. https://doi.org/10.1016/j.scriptamat.2017.02.042.
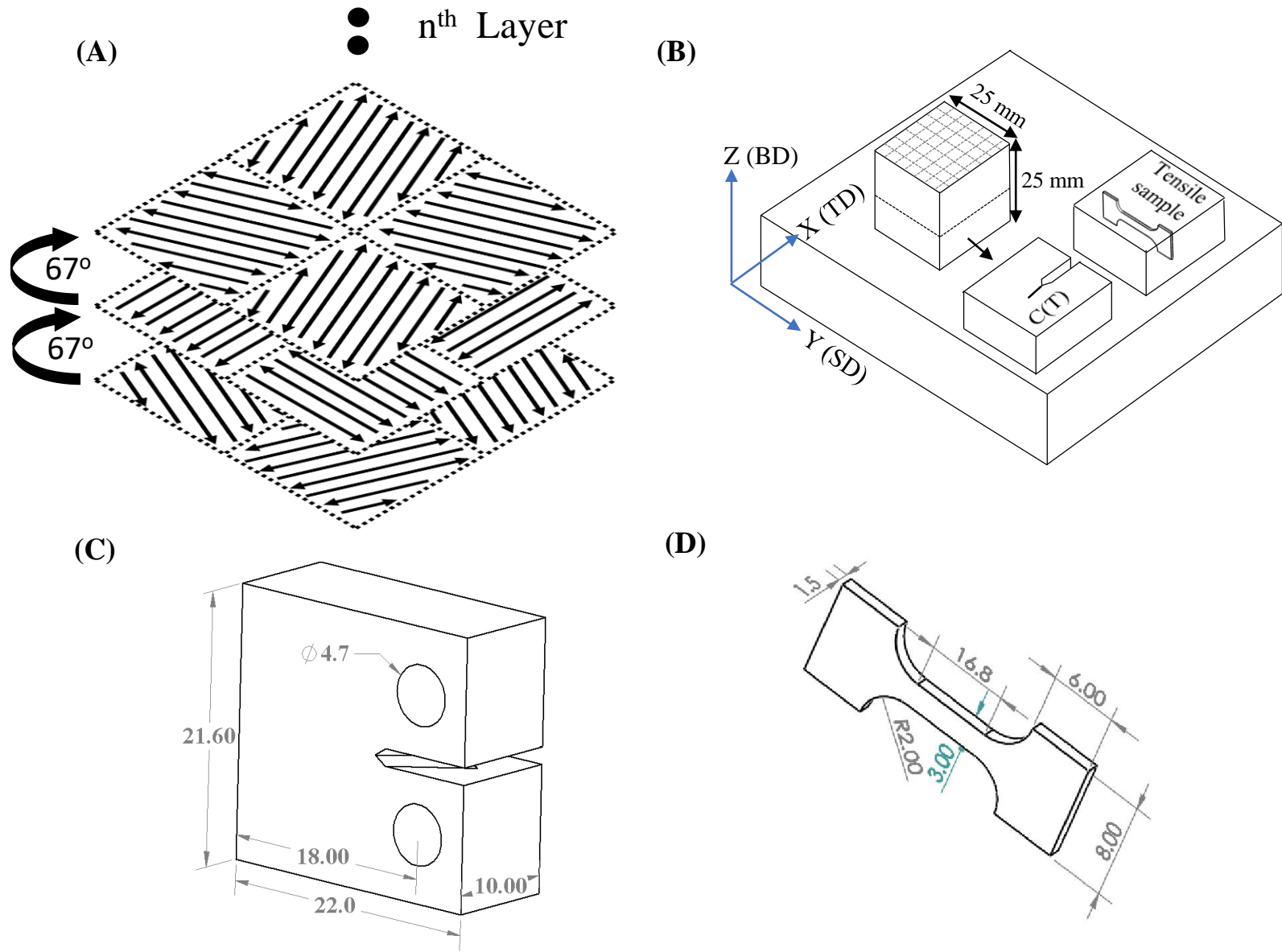
[42] B. Yin, S. Yoshida, N. Tsuji, W.A. Curtin, Yield strength and misfit volumes of NiCoCr and implications for short-range-order, Nat Commun. 11 (2020) 2507. https://doi.org/10.1038/s41467-020-16083-1.

[43] D. Kuhlmann-Wilsdorf, Theory of work hardening 1934-1984, Metallurgical Transactions A. 16 (1985) 2091–2108. https://doi.org/10.1007/BF02670414.

[44] S.-H. Li, Y. Zhao, U. Ramamurty, Role of the solidification cells on the yield strength of the Al-Si-Mg alloy manufactured using laser powder bed fusion: A micropillar compression study, Scr Mater. 234 (2023) 115566. https://doi.org/10.1016/j.scriptamat.2023.115566.

[45] S.-H. Li, Y. Zhao, J. Radhakrishnan, U. Ramamurty, A micropillar compression investigation into the plastic flow properties of additively manufactured alloys, Acta Mater. 240 (2022) 118290. https://doi.org/10.1016/j.actamat.2022.118290.

[46] E. Welsch, D. Ponge, S.M. Hafez Haghighat, S. Sandlöbes, P. Choi, M. Herbig, S. Zaefferer, D. Raabe, Strain hardening by dynamic slip band refinement in a high-Mn lightweight steel, Acta Mater. 116 (2016) 188–199. https://doi.org/10.1016/j.actamat.2016.06.037.

[47] W. Woo, J.S. Jeong, D.K. Kim, C.M. Lee, S.H. Choi, J.Y. Suh, S.Y. Lee, S. Harjo, T. Kawasaki, Stacking Fault Energy Analyses of Additively Manufactured Stainless Steel 316L and CrCoNi Medium Entropy Alloy Using In Situ Neutron Diffraction, Sci Rep. 10 (2020). https://doi.org/10.1038/s41598-020-58273-3.

[48] Y. Ikeda, F. Körmann, I. Tanaka, J. Neugebauer, Impact of chemical fluctuations on stacking fault energies of CrCoNi and CrMnFeCoNi high entropy alloys from first principles, Entropy. 20 (2018) 655. https://doi.org/10.3390/e20090655.

[49] F.C. Puosso, G. Bertoli, F.G. Coury, A Hall–Petch study of the high toughness Cr40Co30Ni30 multi-principal element alloy, J Mater Res. 38 (2023) 215–227. https://doi.org/10.1557/s43578-022-00729-5.

[50] Y. Song, T. Li, X. Fu, Z. Zhang, G. Sheng, Y. Zhu, Y. Lu, Q. Yu, Dislocation-twin interaction in medium entropy alloy containing a high density of oxygen interstitials, J Alloys Compd. 947 (2023) 169522. https://doi.org/10.1016/j.jallcom.2023.169522.

[51] J.-Y. Lee, Y.M. Koo, S. Lu, L. Vitos, S.K. Kwon, The behaviour of stacking fault energy upon interstitial alloying, Sci Rep. 7 (2017) 11074. https://doi.org/10.1038/s41598-017-11328-4.

[52] J.-Y. Lee, Y.M. Koo, S. Lu, L. Vitos, S.K. Kwon, The behaviour of stacking fault energy upon interstitial alloying, Sci Rep. 7 (2017) 11074. https://doi.org/10.1038/s41598-017-11328-4.

[53] I. Moravcik, V. Hornik, P. Minárik, L. Li, I. Dlouhy, M. Janovska, D. Raabe, Z. Li, Interstitial doping enhances the strength-ductility synergy in a CoCrNi medium entropy alloy, Materials Science and Engineering: A. 781 (2020). https://doi.org/10.1016/j.msea.2020.139242.

[54] M. Klimova, D. Shaysultanov, A. Semenyuk, S. Zherebtsov, G. Salishchev, N. Stepanov, Effect of nitrogen on mechanical properties of CoCrFeMnNi high entropy alloy at room and cryogenic temperatures, (2020). https://doi.org/10.1016/j.jallcom.2020.156633.

[55] I. Moravcik, H. Hadraba, L. Li, I. Dlouhy, D. Raabe, Z. Li, Yield strength increase of a CoCrNi medium entropy alloy by interstitial nitrogen doping at maintained ductility, Scr Mater. 178 (2020) 391–397. https://doi.org/10.1016/j.scriptamat.2019.12.007.

[56] X. Liu, S. Zhang, H. Feng, J. Wang, P. Jiang, H. Li, F. Yuan, X. Wu, Outstanding fracture toughness combines gigapascal yield strength in an N-doped heterostructured medium-entropy alloy, Acta Mater. 255 (2023). https://doi.org/10.1016/j.actamat.2023.119079.

[57] B. Han, C. Zhang, K. Feng, Z. Li, X. Zhang, Y. Shen, X. Wang, H. Kokawa, R. Li, Z. Wang, P.K. Chu, Additively manufactured high strength and ductility CrCoNi medium entropy alloy with hierarchical microstructure, Materials Science and Engineering A. 820 (2021). https://doi.org/10.1016/J.MSEA.2021.141545.

[58] R.O. Ritchie, A.W. Thompson, On macroscopic and microscopic analyses for crack initiation and crack growth toughness in ductile alloys, Metallurgical Transactions A. 16 (1985) 233–248. https://doi.org/10.1007/BF02815305.

[59] J.W. Hutchinson, Singular behaviour at the end of a tensile crack in a hardening material, J. Mcch. Phys. Solids. 16 (1968) 13–31.

[60] J.R. Rice, G.F. Rosengren, Plane strain deformation near a crack tip in a power-law hardening material, J. Me&. Phys. Solids. 16 (1968) 1–12.

**Table 1:** The mechanical properties of laser powder bed fusion (LPBF) processed CrCoNi.

Temperature (K)	Yield strength, σ_Y (MPa)	Ultimate tensile strength, σ_u (MPa)	Strain hardening exponent, n	Energy release rate, J_{Ic} (kJ/m^2)	Fracture toughness, K_{JIc} (MPa√m)
298	691 ± 9.2	926 ± 15.2	0.19	136 ± 43	183.7 ± 28
77	944 ± 5.6	1382 ± 11	0.22	118 ± 14	176.3 ± 11

Fig. 1. (A) Scanning strategy for LPBF process of CrCoNi samples. (B) The relative orientation of the compact-tension C(T) and tensile specimens with respect to the build plate, where the Z-axis is parallel to the build direction (BD), the Y-axis to scan direction (SD), and the X-axis to the transverse direction (TD). (C) Dimensions of C(T) sample and (D) tensile specimen dimensions. In Figs. C and D, all the dimensions are in mm.
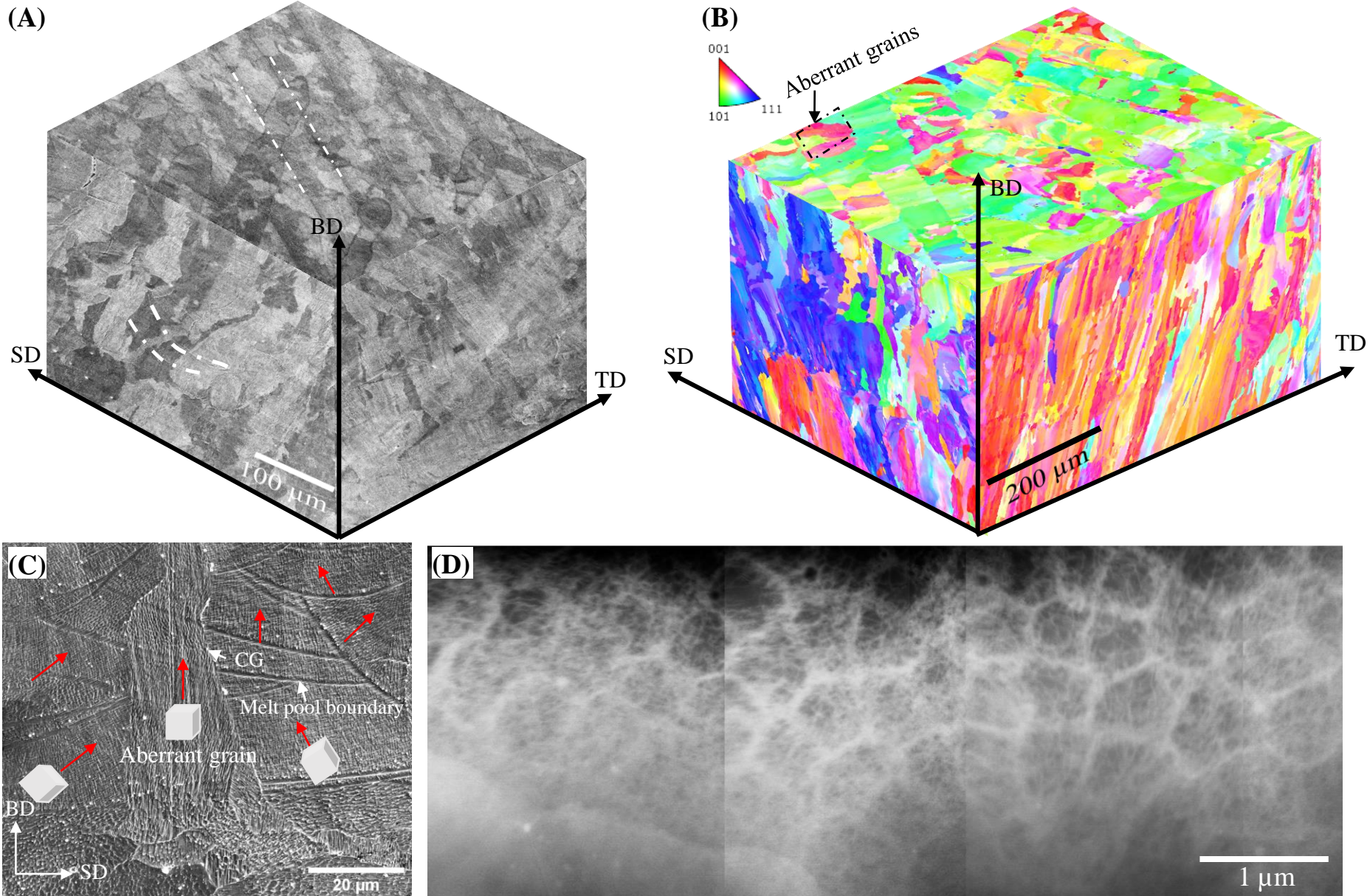
Fig. 2. (A) Representative 3D microstructure showing laser scan tracks (white dotted lines) on the plane parallel to the build direction, BD, and melt pool on the planes perpendicular to the build direction, *i.e.*, the scan and transverse directions, SD and TD. (B) 3-D representative inverse pole figure (IPF) map obtained by electron back-scattered diffraction (EBSD) shows multiple grains inside the laser scan tracks and columnar grains on SD and TD planes. (C) High-magnification etched image shows an aberrant grain growing across multiple melt pool boundaries. The red arrows indicate the direction of the growth of cellular structure inside the melt pools. (D) Transmission electron microscopy (TEM) image shows the cellular network of dislocations inside the grains.
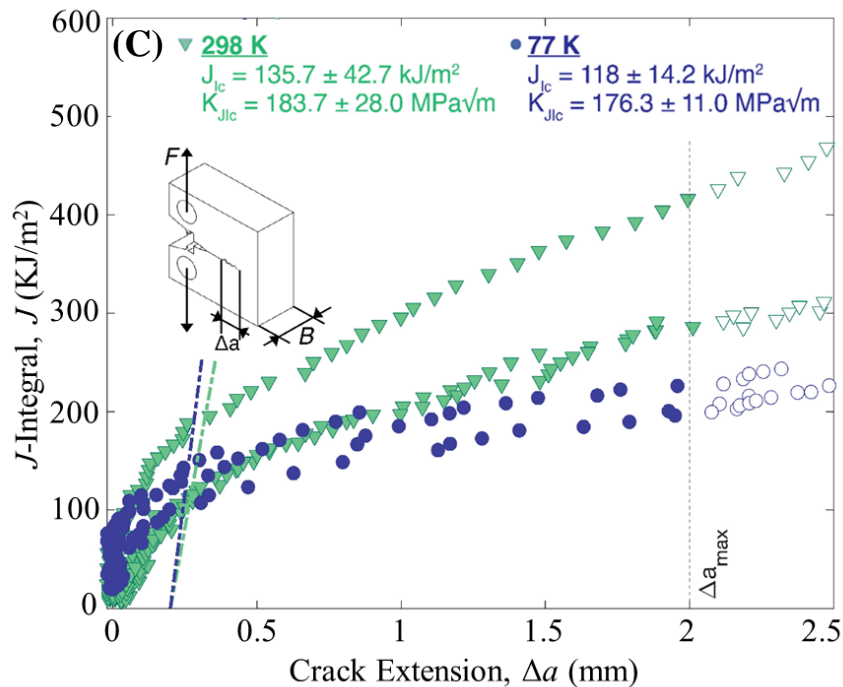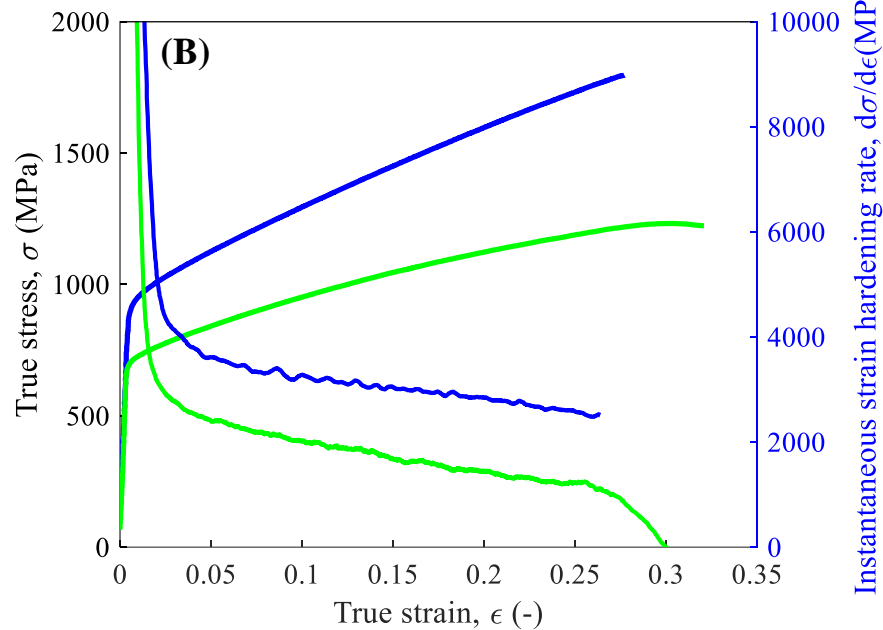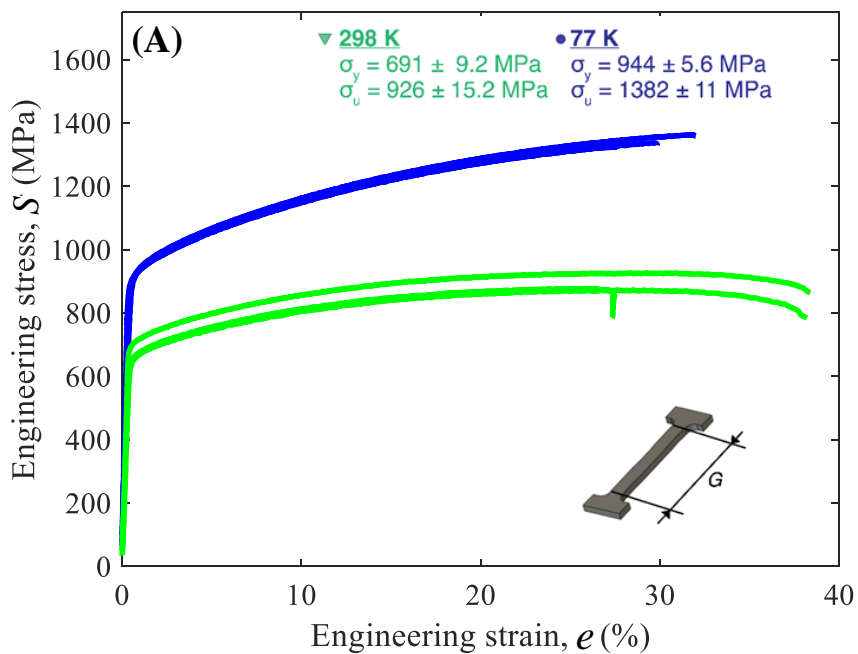
Fig. 3. (A) Engineering stress, *S*, *vs.* engineering strain, *e* curves obtained by uniaxial tensile tests of specimens at 298 K and 77 K. (B) Representative true stress, σ *vs.* true strain, ε, and instantaneous strain hardening rate, dσ/dε *vs.* true strain, ε plots for specimens tested at 298 and 77 K. (C) Crack-resistance curves (R-curves) of LPBF CrCoNi specimens tested at 298 K and 77 K.
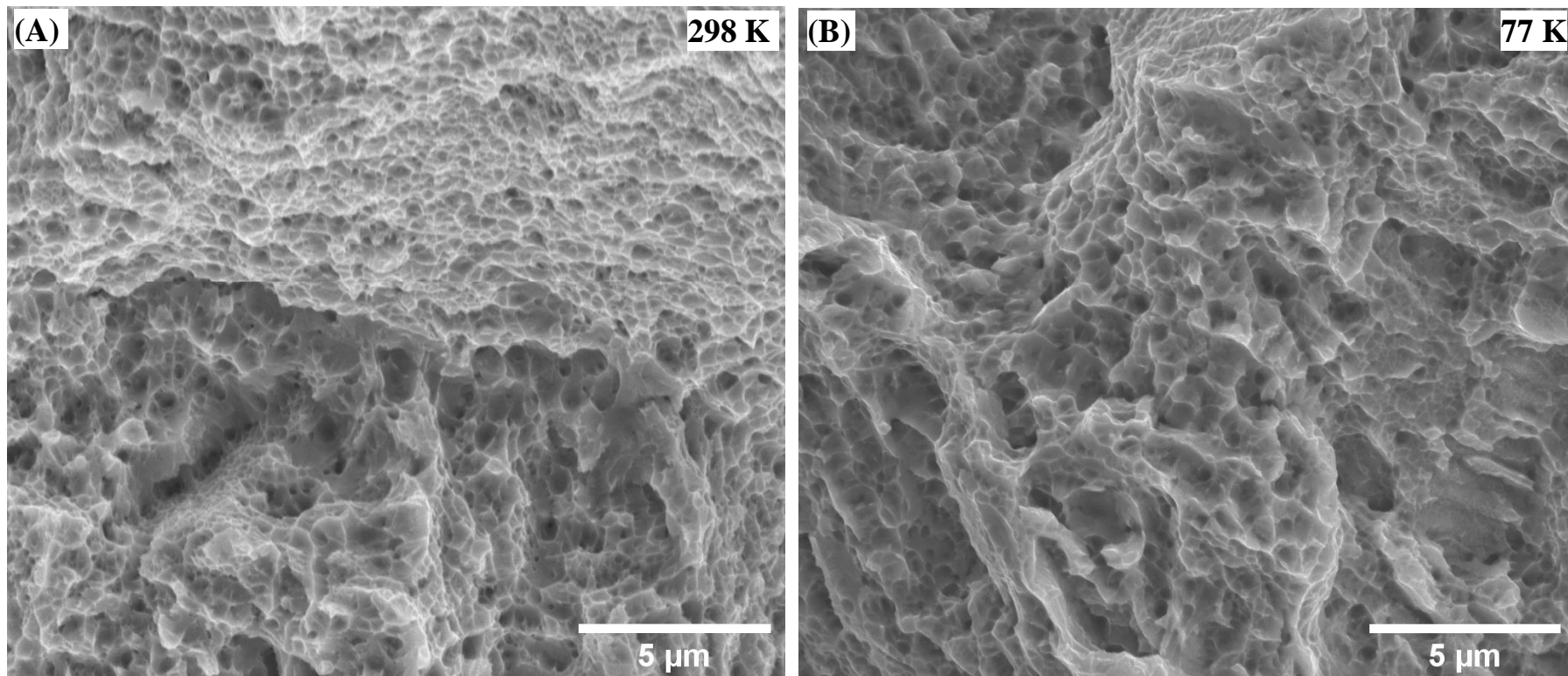
Fig. 4. Scanning electron microscopy (SEM) fractographs showing microvoid coalescence in the tensile specimens fractured at (A) 298 K and (B) 77 K.
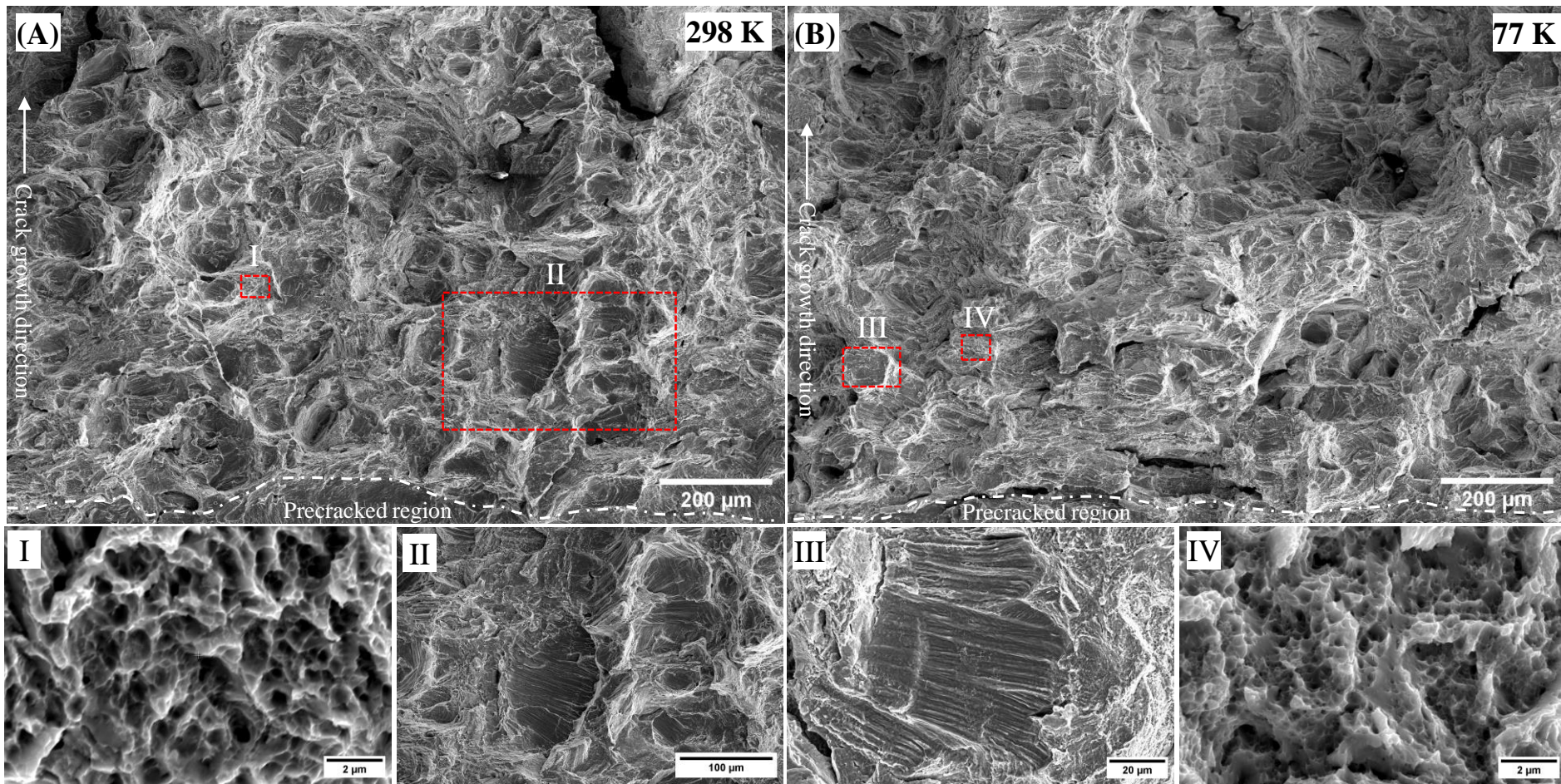
Fig. 5. SEM fractographs of C(T) specimens after fracture toughness measurements at (A) 298 K and (B) 77 K. The magnified image of regions indicated by red dotted lines, I and II, III, and IV in Figs. A and B are at the bottom of the image.
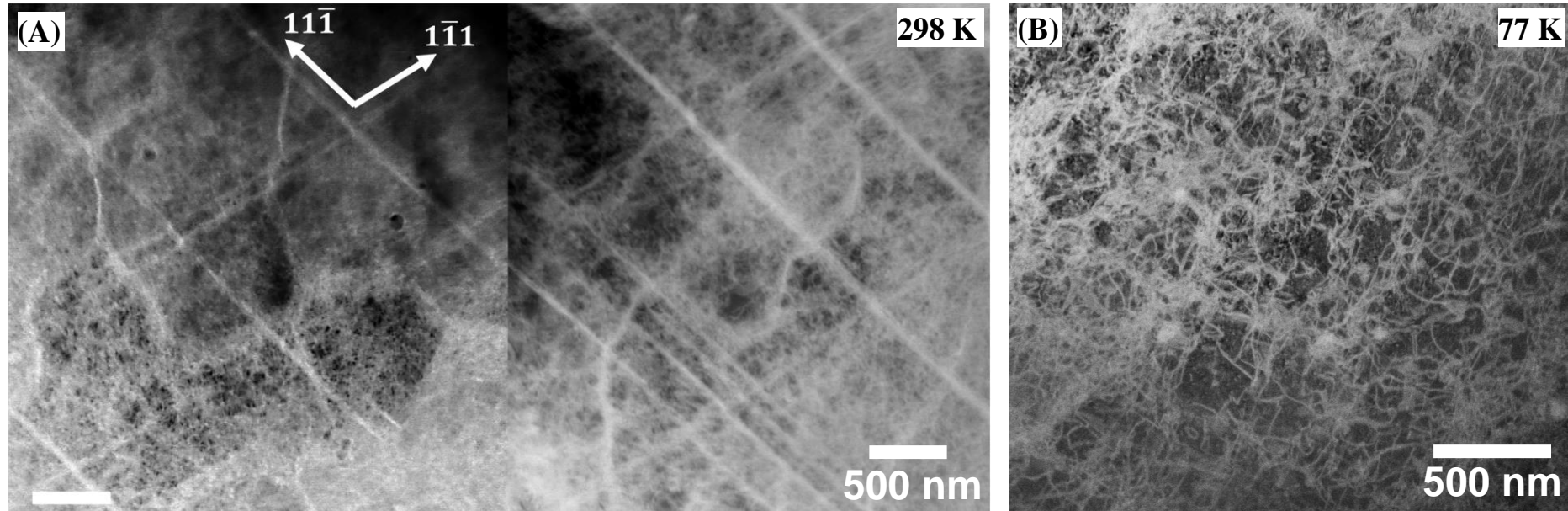
Fig. 6. TEM images showing (A) <111> planar slip cutting through cellular boundaries inside the crack-tip plastic zone of specimen tested at 298 K. (B) Cellular structure and relatively higher dislocation density inside the crack-tip plastic zone of the specimen tested at 77 K.
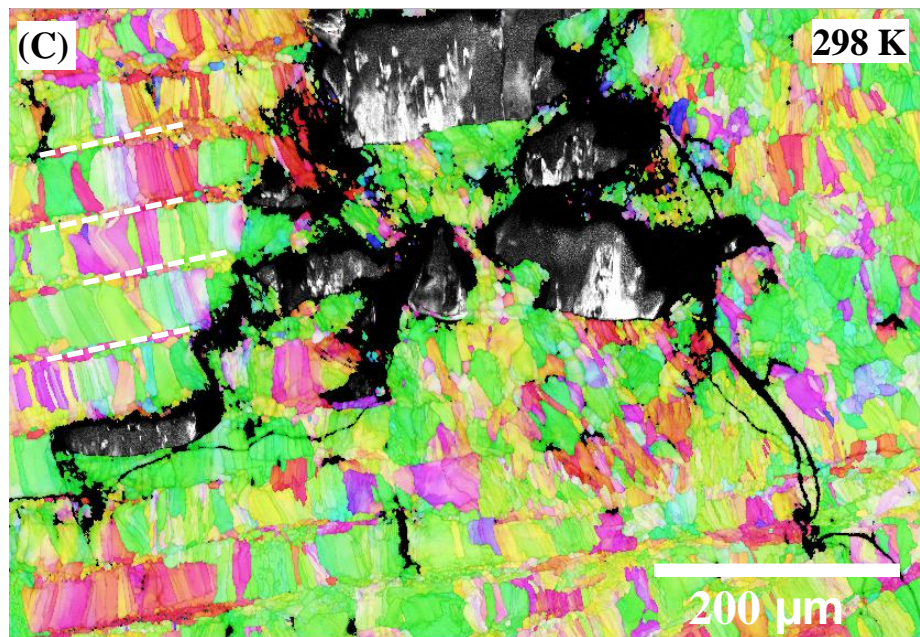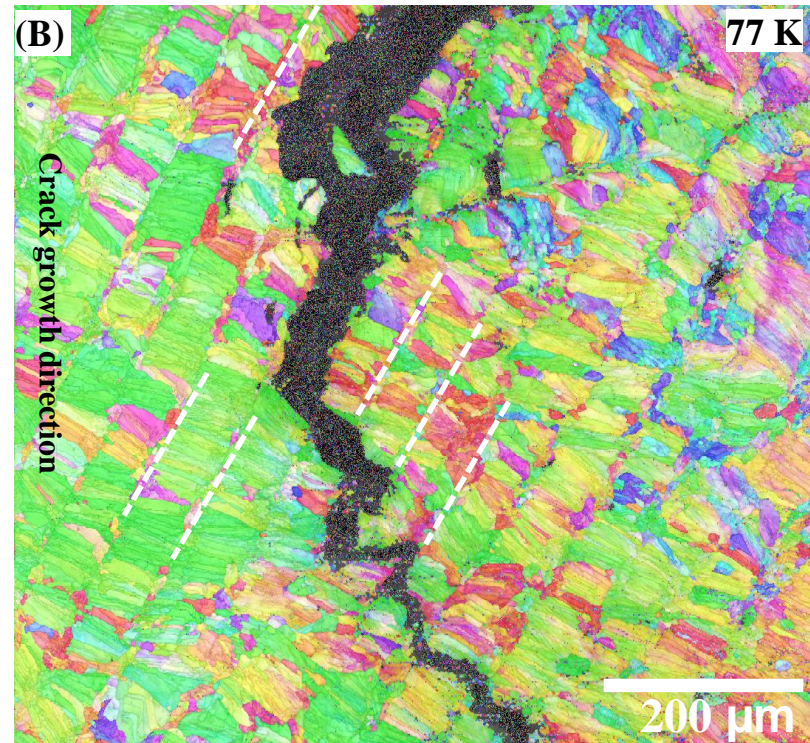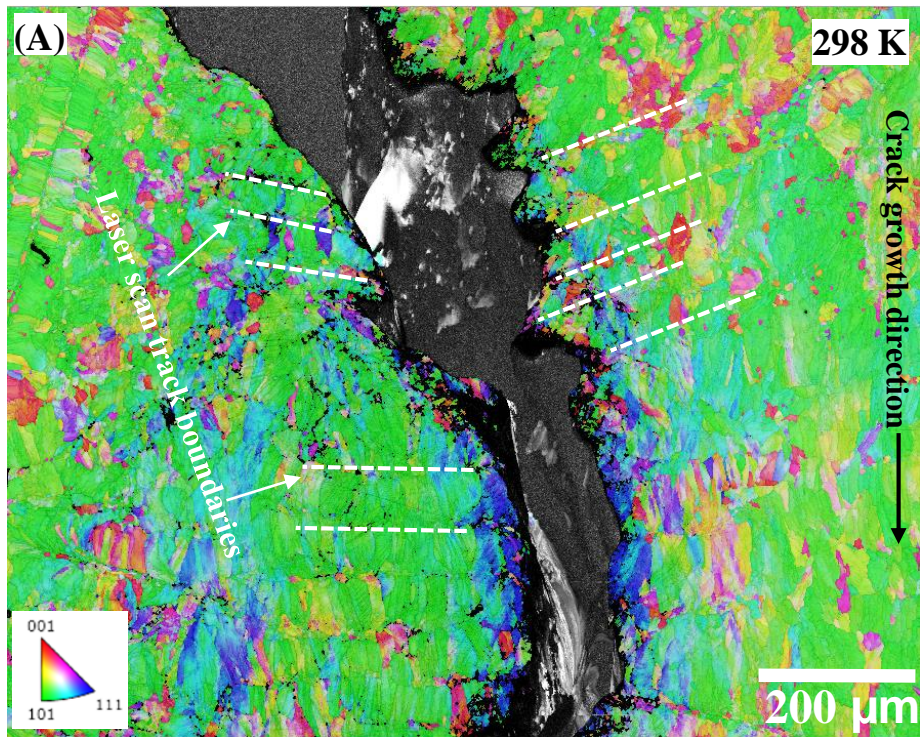
Fig. 7. Electron backscattered (EBSD) inverse pole figure (IPF) maps showing the crack path during fracture by overload and the interaction of the crack with the microstructure. The IPF maps of the location where crack growth starts during the fracture at (A) 298 K, (B) 77 K. (C) IPF map of the location where the crack was arrested during fracture toughness test 298 K. In all three specimens, the orientation of the laser scan track near the crack tip is different owing to the 67° scan rotation between the layers with a chessboard pattern of 4×4 mm^2 islands. In each figure, the white dotted lines in images show the boundary of laser scan tracks. The fracture toughness, K_{JIc} of these specimens are (A) 216 MPa√m, (B) 185 MPa√m, and (C) 167 MPa√m.
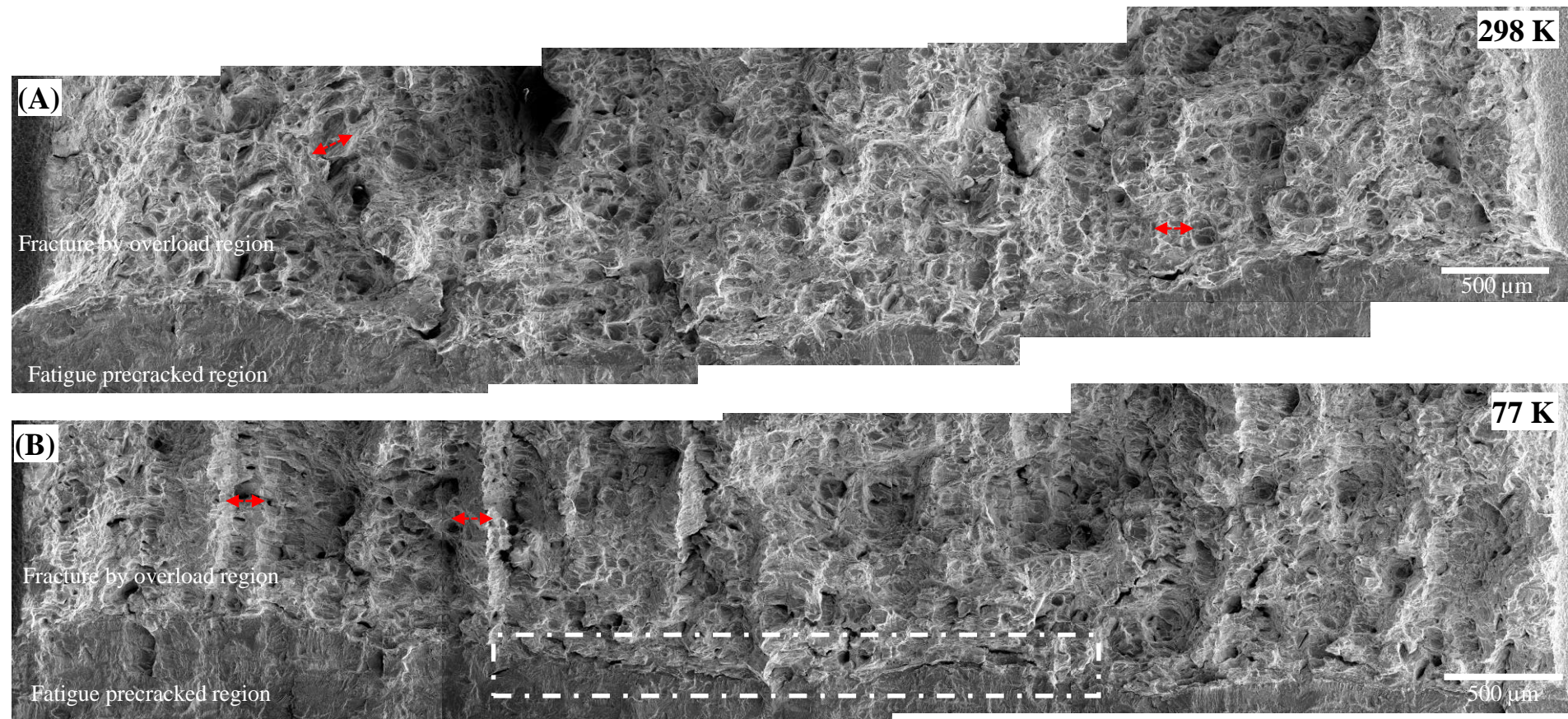
Fig. 8. SEM fractographs showing the tortuosity of the crack path arising from laser scan tracks in specimens tested at (A) 298 K and (B) 77 K. In Fig. (B), the rectangle with white dotted lines shows secondary cracks in the stretch zone, indicating extrinsic toughening. The red double arrow lines show the remanent of laser scan tracks after the fracture.
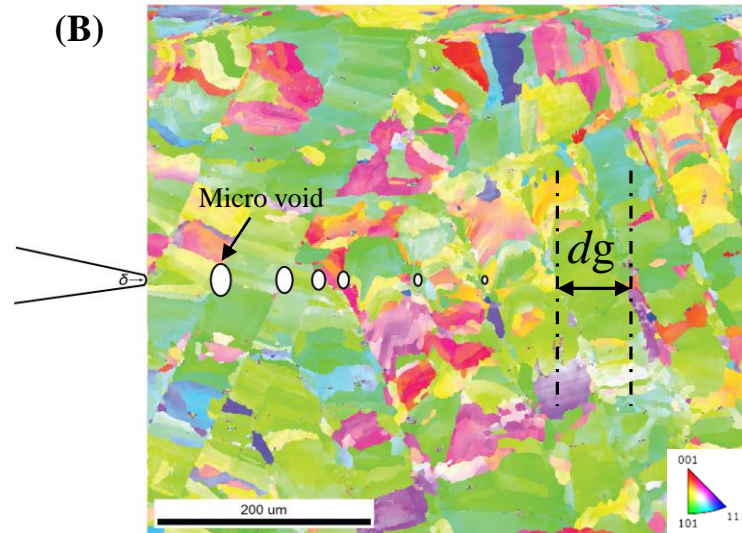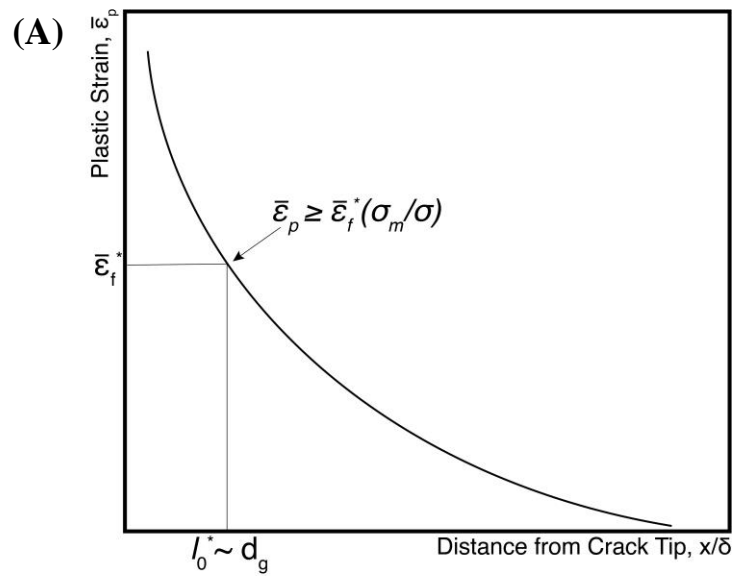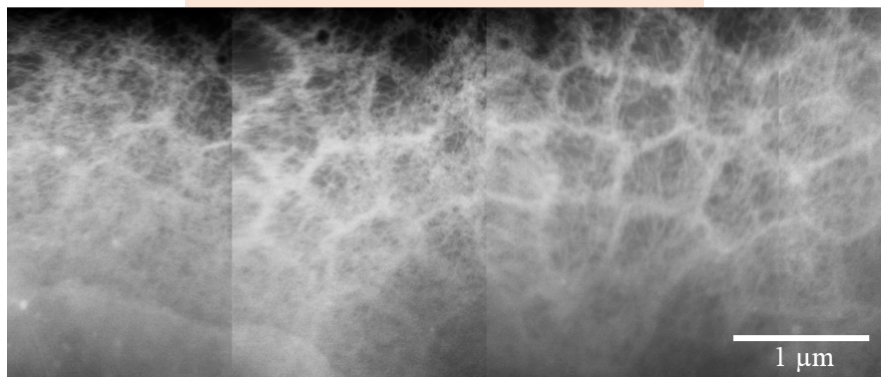
Fig. 9. The stress-state modified critical strain-controlled model for ductile fracture by microvoid coalescence. (A) The plot shows the HRR solutions for the plastic stain, ε_p, distribution at a distance x ahead of the crack tip for a particular crack-tip opening displacement, δ, in a nonlinear elastic power-law hardening material. The criterion is relevant to the fracture of the CrCoNi by microvoid coalescence; it requires that the local plastic strain $\bar{\varepsilon}_p$ exceeds a fracture strain $\bar{\varepsilon}_f$ over a characteristic distance, l_o^*, which is related to the characteristic microstructural length scale, dg. The estimation based on the micromechanics model indicates that the laser scan track's width, h is the characteristic microstructural length scale, *i.e.*, dg ~ h. (B) The IPF map indicating the boundary of the laser scan track as a preferred location for the nucleation of the microvoid.
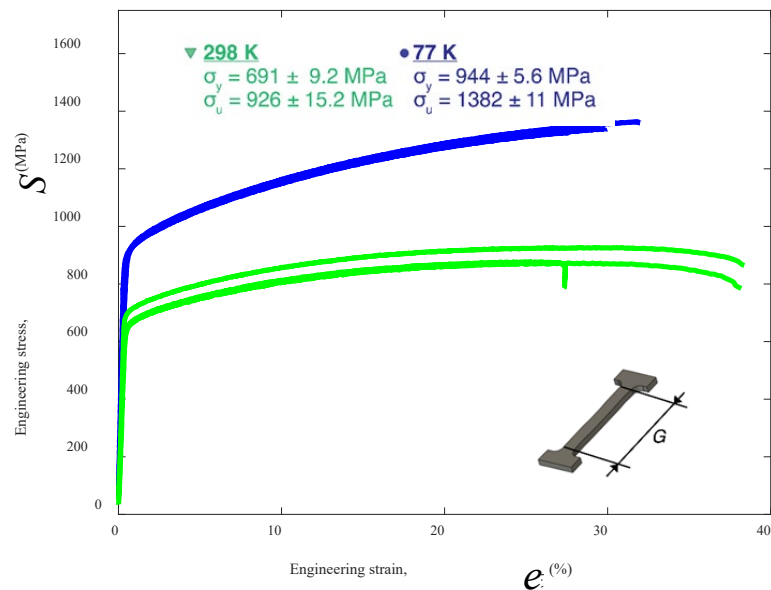
Additive manufactured CrCoNi
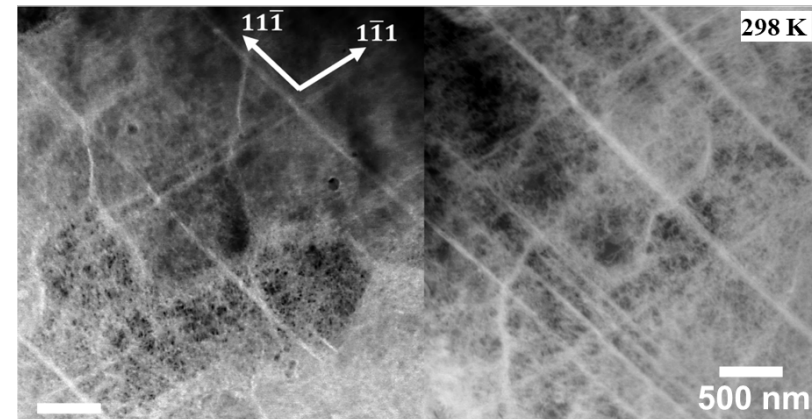
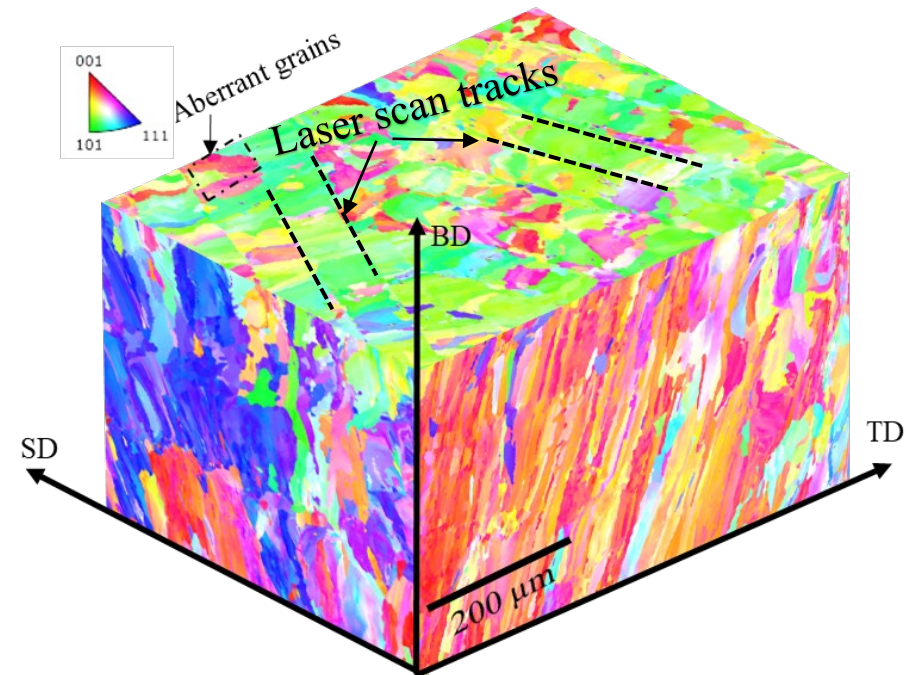## Hierarchical micro-and mesostructures

Dislocation cellular structure

1 μm

Texture and grain morphology

Aberrant grains

Laser scan tracks

001 101 111

BD

SD

TD

200 μm

Tensile properties

▼ 298 K
σ_y = 691 ± 9.2 MPa
σ_u = 926 ± 15.2 MPa

• 77 K
σ_y = 944 ± 5.6 MPa
σ_u = 1382 ± 11 MPa

S (MPa)

Engineering stress,

Engineering strain, e (%)

G

Fracture toughness

▼ 298 K
J_{Ic} = 135.7 ± 42.7 kJ/m²
K_{JIc} = 183.7 ± 28.0 MPa√m

• 77 K
J_{Ic} = 118 ± 14.2 kJ/m²
K_{JIc} = 176.3 ± 11.0 MPa√m

J-Integral, J (KJ/m²)

Crack Extension, Δa (mm)

F

Δa

B

Δa_{max}

Strengthening mechanism

$11\bar{1}$ $1\bar{1}1$

298 K

500 nm

Toughening mechanism

Crack growth direction

200